

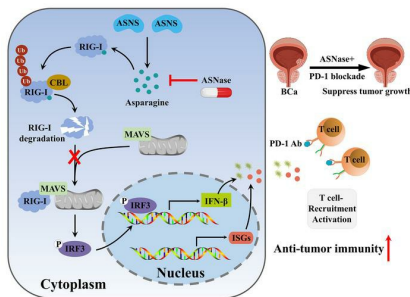
Asparagine drives immune evasion in bladder cancer via RIG-I stability and type I IFN signaling

Wenjie Wei, ... , Xu Zhang, Yan Huang

J Clin Invest. 2025. <https://doi.org/10.1172/JCI186648>.

Research In-Press Preview Cell biology Immunology

Graphical abstract



Find the latest version:

<https://jci.me/186648/pdf>



30 **Abstract**

31 Tumor cells often employ many ways to restrain type I interferon signaling to evade
32 immune surveillance. However, whether cellular amino acid metabolism regulate this
33 process remains unclear and its effects on antitumor immunity are relatively unexplored.
34 Here, we find that asparagine inhibits IFN-I signaling and promotes immune escape in
35 bladder cancer. Depletion of asparagine synthetase (ASNS) strongly limits in vivo
36 tumor growth in a CD8⁺ T cell-dependent manner and boosts immunotherapy efficacy.
37 Moreover, clinically approved ASNase synergizes with anti-PD-1 therapy in
38 suppressing tumor growth. Mechanistically, asparagine can directly bind to RIG-I and
39 facilitate CBL-mediated RIG-I degradation, thereby suppressing IFN signaling and
40 antitumor immune responses. Clinically, tumors with higher ASNS expression show
41 decreased responsiveness to ICIs therapy. Together, our findings uncover asparagine as
42 a natural metabolite to modulate RIG-I-mediated IFN-I signaling, providing the basis
43 for developing the combinatorial use of ASNase and anti-PD-1 for bladder cancer.

44
45
46
47
48
49
50
51
52
53
54
55
56
57
58

59 **Introduction**

60 Bladder cancer is one of the most prevalent tumors in the urinary system and is
61 responsible for nearly 165,000 deaths every year worldwide (1). Approximately 25%
62 of patients present with muscle invasive disease and the relative 5-year overall survival
63 rate of advanced-stage bladder cancer is low, with limited therapeutic advances (2, 3).
64 Radical cystectomy and cisplatin-based chemotherapy are recommended for the
65 standard treatment option for muscle-invasive bladder cancer (MIBC) (4). In recent
66 years, immune checkpoint inhibitors (ICIs) have achieved tremendous clinical
67 breakthroughs in cancer immunotherapy (5, 6). Though ICIs have shown durable
68 responses in a subset of patients with bladder cancer, the overall response rate is only
69 ~15–25% (7, 8), which increases the demand for biomarkers of response and effective
70 targeted therapies to enhance ICIs therapy.

71

72 Emerging evidence indicates that the tumor microenvironment (TME) is a
73 complex system that determines the occurrence of tumor immune responses (9, 10).
74 CD8+ T cells play a central role in cancer immunotherapy and elicit antitumor activity
75 by directly recognizing and killing tumor cells (11, 12). Patients with high CD8+ T cells
76 infiltration in TME are associated with a survival benefit in several tumor types and
77 better response to immunotherapy (13). Previous studies have reported that type
78 I Interferon (IFN-I) are essential for activating adaptive immune response and play a
79 crucial role in CD8+ T cells infiltration and immunogenic tumor rejection (14, 15).
80 Given that RIG-I-like receptors (RLRs) are critical for activating the IFNs pathway and
81 triggering immunogenic cell death, stimulation of retinoic acid-inducible gene-I (RIG-
82 I) or melanoma differentiation-associated gene 5 (MDA5) signaling has emerged as a
83 strategy for antitumor immunity (16, 17). However, tumor cells often employ multiple
84 strategies to evade immunosurveillance by inhibiting RLRs-mediated signaling
85 pathway (18, 19). Therefore, a better comprehension of the regulatory mechanism of
86 RLRs-mediated IFNs in tumor immunity is of great clinical importance for patients
87 with bladder cancer.

88 Tremendous efforts have recently been dedicated to the investigation of metabolic
89 reprogramming in the regulation of tumor immunity (20-22). Among them, amino acid
90 metabolism has attracted widespread attention. Asparagine synthetase (ASNS)
91 catalyzes the conversion of aspartate to asparagine in an ATP-dependent reaction.
92 Currently, L-asparaginase (ASNase), a drug that deprives plasma asparagine, is
93 considered to be a first-line therapy for childhood acute lymphoblastic leukemia (ALL)
94 (23). Accumulating studies have revealed that asparagine is tightly linked to the
95 activation and differentiation of CD8⁺ T cells, thereby affecting antitumoral
96 functionality (24-26). In addition, ASNS is always elevated in many cancer types and
97 increased asparagine contributes to cancer cell survival and metastasis (27-29).
98 Nonetheless, the specific roles of asparagine metabolism on the cancer cell-intrinsic
99 functions and on the regulation of RLRs-mediated antitumor immunity have not been
100 explored.

101

102 Here, we report that asparagine restriction enhances RIG-I mediated IFNs
103 signaling and potentiates antitumor immunity in bladder cancer. Clinically, ASNS is
104 upregulated and is associated with a poor response to immunotherapy in bladder cancer.
105 Limiting asparagine by knockdown of ASNS or treatment with ASNase increases
106 intratumoral CD8⁺ T cells infiltration and effector function, thus boosting the efficacy
107 of PD-1 blockade. Mechanistically, asparagine can directly facilitate the interaction
108 between E3 ligase CBL and RIG-I, consequently inducing RIG-I degradation to
109 suppress IFN signaling, thereby limiting antitumor immune responses. Our study
110 highlights a role of asparagine in regulating RIG-I stability and connect asparagine
111 metabolism to the IFN-I signaling that modulates antitumor immunity, suggesting that
112 targeting ASNS is a promising approach to enhance immunotherapy for bladder cancer.

113

114 **Results**

115 **Asparagine restriction attenuates tumor growth in an immunity-dependent**
116 **manner**

117 Previous study reports that ASNS function as a critical enzyme that catalyzes the
118 biosynthesis of asparagine from aspartate in an ATP-dependent reaction (23). To
119 interrogate the biological functions of ASNS on cancer cells, we knocked down the
120 *Asns* gene in two malignant mouse bladder cancer cell lines (MB49 and MBT2) and a
121 human bladder cancer cell lines UMUC3 (Supplemental Figure 1, A and B). To our
122 surprise, loss of ASNS did not alter the in vitro growth rates and migration abilities of
123 tumor cells (Supplemental Figure 1, C-F). Consistent with this, we found that
124 asparagine also had no obvious difference on the proliferation abilities of bladder cancer
125 cells compared with the control cells (Supplemental Figure 1G).

126

127 To investigate the effect of ASNS on tumor growth in vivo, ASNS-deficient mouse
128 bladder cancer cells were injected subcutaneously into the flanks of
129 immunocompromised mice. Our results demonstrated that loss of ASNS had no effect
130 on tumor growth in BALB/c nude mice (Figure 1, A and B, and Supplemental Figure 1,
131 H and I). To determine the involvement of the immune system, we inoculated ASNS-
132 deficient and control bladder cancer cells into syngeneic mice hosts. Of note, silencing
133 of ASNS inhibited tumor growth in both immunocompetent mice (Figure 1, C and D).
134 To assess the effect of asparagine on the tumor growth in vivo, we subcutaneously
135 injected murine bladder cancer cells into mice, and followed by oral administration of
136 PBS or asparagine, respectively. We observed no significant difference in
137 immunocompromised mice administrated with asparagine (Figure 1, E and F). However,
138 asparagine treatment promoted tumor growth in both immunocompetent murine
139 bladder cancer models (Figure 1, G and H). Collectively, these data suggest that
140 asparagine restriction could suppress tumor growth, which requires the presence of an
141 intact immune system.

142

143 **Knockdown of ASNS potentiates recruitment and activation of CD8⁺ T cells**

144 We next attempted to quantify immune effector cells in control and ASNS-deficient
145 bladder tumors by flow cytometry. Gating strategy to analyze the population of immune

146 cells in mouse transplanted tumors was shown in Supplemental Figure 2A. We found
147 that knockdown of ASNS could significantly increase CD8⁺ T cells infiltration in both
148 tumors established by MB49 and MBT2 cells (Figure 2A). However, there were no
149 consistent differences in CD4⁺ T cells and NK cells in both models (Supplemental
150 Figure 3, A-D). Previous studies have shown that T cells exclusion from the tumor
151 parenchyma is one of the mechanisms underlying immunosuppression in the TME and
152 is associated with poor response to current immunotherapies (30, 31). Notably,
153 depletion of ASNS also increased the infiltration of CD8⁺ T cells in tumor parenchyma
154 (Figure 2B) and enhanced their cytokines production including GZMB, TNF- α and
155 IFN- γ (Figure 2, C and D, and Supplemental Figure 2B). On the contrary, asparagine
156 treatment decreased the infiltration of CD8⁺ T cells and impaired function of CD8⁺ T
157 cells to secrete GZMB (Figure 2, E and F, and Supplemental Figure 3E).

158

159 To determine the extent to which ASNS inhibition promoted an antitumor reaction
160 dependent on CD8⁺ T cells in vivo, CD8⁺ T cells were deleted using anti-CD8 antibody
161 (Figure 2G and Supplemental Figure 3, F and G). We found that ASNS deficiency-
162 mediated antitumor function was largely abolished in the CD8⁺ T cell-depleted group
163 (Figure 2, H and I). Collectively, these results indicate that the tumor-suppressive effect
164 of asparagine restriction might be mediated by tumor-infiltrating CD8⁺ T cells.

165

166 **Silencing of ASNS triggers RIG-I-induced type I IFN signaling**

167 To further decipher the mechanism of immunoactivation mediated by ASNS inhibition,
168 we performed RNA-sequencing analysis in ASNS-deficient MBT2 cells (Figure 3A and
169 Supplemental Figure 4A). Gene ontology (GO) analysis and gene set enrichment
170 analysis (GSEA) showed that differentially expressed genes were enriched in biological
171 pathways related with IFN pathway and adaptive immune response process, including
172 response to type I IFN, regulation of T cell mediated cytotoxicity and so on (Figure 3,
173 B and C, and Supplemental Figure 4B). Then, we confirmed the RNA-seq data that
174 knockdown of ASNS elevated the expression of interferon-stimulated genes (ISGs)

175 (e.g., OAS2, OAS3, RIG-I, CCL5 and ISG15) and IFN- β (Figure 3D and Supplemental
176 Figure 4C). We also applied Luminex system multiple immunoassays to detect multiple
177 cytokines and chemokines in cell culture supernatants from ASNS-deficient and control
178 MBT2 cells. Supporting the results obtained in RNA-seq, knockdown of ASNS
179 upregulated the expression of CCL5 and promoted its secretion (Figure 3E), which is
180 robustly correlated with CD8⁺ T cells infiltration in solid tumors (32). Moreover, the
181 secretion levels of IFN- β and CCL5 protein were improved in ASNS-deficient bladder
182 cancer cells by using ELISA (Figure 3F and Supplemental Figure 4D). In contrast,
183 asparagine attenuated the expression of IFN- β and CCL5 in bladder cancer cells
184 (Supplemental Figure 4, E and F).

185

186 Previous studies have reported that several innate sensing pathways can stimulate
187 the induction of type I IFNs. For example, cGAS-STING of dsDNA sensors, RIG-
188 I/MDA5-MAVS of dsRNA sensors and Toll-like receptors (TLR3 and TLR4) of LPS
189 sensors converge at the activation of TANK-binding kinase 1 (TBK1) and interferon
190 regulatory factor 3 (IRF3), triggering the expression of type I IFNs (33). However, type I
191 IFNs mediated by intracellular nucleic acid sensors are a key component to activate the
192 immune system against cancer (34). Therefore, we inhibited the expression of pivotal
193 nucleic acid sensors by shRNA-mediated silencing prior to knocking down ASNS to
194 identify which sensor was essential for ASNS inhibition induced IFN-I activation.
195 Intriguingly, abrogation of MAVS (Figure 3G), but not STING (Supplemental Figure
196 4G), substantially diminished the induction of IFN- β in response to ASNS inhibition.
197 Therefore, we speculated that RIG-I/MDA5-MAVS pathway was essential for IFN-I
198 activation upon ASNS inhibition. Then, we confirmed that knockdown of ASNS was
199 sufficient to enhance IFN- β and CCL5 production following transfection of dsRNA
200 mimic analogue poly (I:C) (Figure 3, H and I, and Supplemental Figure 4H), a synthetic
201 dsRNA analogue (35). Conversely, exogenous asparagine decreased the expression of
202 IFN- β and CCL5 induced by poly(I:C) (Figure 3J and Supplemental Figure 4, I and J).
203 Previous study has been reported that L-asparaginase (ASNase) is a core component of

204 the chemotherapy regimen for childhood acute lymphoblastic leukemia, which could
205 participate in the catabolism of asparagine (36). Notably, the expression levels of IFN-
206 β and CCL5 were higher in bladder cancer cells treated with ASNase (Figure 3K and
207 Supplemental Figure 4K).

208

209 Giving that endogenous dsRNAs is responsible for activating the cytoplasmic
210 dsRNA sensors and triggering IFN-I response in several types of cancer cells (37, 38).
211 We investigated the level of endogenous dsRNAs using a dsRNA-specific antibody and
212 found that the depletion of ASNS substantially had no obvious effect on the level of
213 endogenous dsRNA (Supplemental Figure 5A). Of note, knockdown of ASNS or
214 asparagine could alter the expression of IFN- β and CCL5 upon poly(I:C) treatment. We
215 speculated that ASNS loss or asparagine exerted their function by mediating dsRNA
216 sensors, but not dsRNA production. To further explored whether ASNS inhibition
217 activated RIG-I/MDA5 signaling and we found that knockdown of ASNS upregulated
218 RIG-I expression and promoted the phosphorylation of IRF3 proteins, a transcription
219 factor that induces IFN expression (Figure 3L and Supplemental Figure 5B). We also
220 observed a reduction of the RIG-I expression under asparagine addition (Supplemental
221 Figure 5C), but not aspartate (Supplemental Figure 5D). In addition, we demonstrated
222 that poly (I:C) intensely increased the expression of RIG-I and p-IRF3 protein, which
223 could be reduced by asparagine in bladder cancer cells (Figure 3M and Supplemental
224 Figure 5E). Importantly, the upregulation of RIG-I and p-IRF3 protein levels induced
225 by ASNS knockdown was considerably abolished by asparagine (Figure 3N and
226 Supplemental Figure 5F). Collectively, these findings reveal that ASNS inhibition could
227 activate RIG-I-induced IFN- β signaling in bladder cancer.

228

229 To further investigate whether IFN- β signaling is essential for ASNS inhibition-
230 elicited antitumor immunity, we genetically abrogated IFN- β production in bladder
231 cancer cells (Supplemental Figure 6A), which completely reversed ASNS deficiency-
232 mediated inhibition of tumor growth in vivo (Figure 3, O and P, and Supplemental

233 Figure 6, B and C). In line with this, we blocked IFN- β signaling using anti-IFNAR1
234 antibody in vivo and also found that treatment with anti-IFNAR1 antibody markedly
235 restored the growth retardation of ASNS-deficient tumors in C57BL/6 mice
236 (Supplemental Figure 6, D-G). Taken together, these results strongly indicate that IFN-
237 β signaling plays a pivotal role in ASNS deficiency-mediated antitumor immune
238 responses.

239

240 **Cellular asparagine abundance affects RIG-I protein stability**

241 We next sought to investigate the mechanism involved in ASNS inhibition-induced
242 IFN-I pathway activation. The aforementioned results have depicted that ASNS
243 inhibition could elevate the expression levels of mRNA and protein of RIG-I. Of note,
244 previous studies have reported that RIG-I, as a ISGs, could be strongly induced by IFNs
245 in a positive feedback manner (39, 40). Therefore, we inhibited the expression of MAVS
246 by shRNA before knocking down ASNS to block the feedback effect of the IFN-I
247 signaling on RIG-I, and found that knockdown of ASNS upregulated the expression of
248 RIG-I protein, but not mRNA (Figure 4, A and B). Consistently, asparagine only
249 decreased the level of RIG-I protein (Figure 4, C and D). Then, we transfected Flag-
250 RIG-I plasmids in HEK293T cells and found that asparagine treatment attenuated the
251 RIG-I and IFN- β expression (Figure 4E). Therefore, we hypothesized that RIG-I
252 upregulation induced by ASNS inhibition was achieved by monitoring its protein layer.

253

254 Subsequently, we conducted CHX experiment and found that silencing of ASNS
255 significantly extended the half-life of RIG-I protein, indicating that ASNS knockdown
256 inhibited the degradation of RIG-I (Figure 4, F-I). In addition, the reduction of RIG-I
257 protein induced by asparagine was abolished by proteasome inhibitor MG132 in
258 bladder cancer cells, but not lysosome inhibitor CQ (Figure 4, J and K). Co-
259 immunoprecipitation experiments indicated that asparagine markedly increased K48-
260 linked ubiquitination of RIG-I (Figure 4L), whereas ASNS deficiency decreased K48-
261 linked ubiquitination of RIG-I (Figure 4M). Collectively, these data suggest that

262 knockdown of ASNS upregulates RIG-I expression by protecting it from degradation.

263

264 **Asparagine binds to RIG-I and enhances its ubiquitination by CBL**

265 Increasing evidences indicate that the E3 ubiquitin ligases RNF122, RNF125, STUB1
266 and CBL play pivotal role in the RIG-I degradation via K48-linked ubiquitination (19,
267 41). We further determined how asparagine affects K48-linked polyubiquitination and
268 suppression of RIG-I. Co-immunoprecipitation experiments indicated that asparagine
269 promoted the association of CBL with RIG-I but not RNF122, RNF125, and STUB1 in
270 mammalian overexpression system (Figure 5A and Supplemental Figure 7, A-C).
271 Importantly, we demonstrated that asparagine could promote the polyubiquitination of
272 RIG-I protein in CBL-overexpressed cells (Figure 5B). In contrast, CBL knockdown
273 ablated the promotion of RIG-I polyubiquitination elicited by asparagine
274 (Supplemental Figure 7D). Even though asparagine may trigger certain metabolic
275 processes that can influence CBL-mediated RIG-I ubiquitination, it is attractive to
276 detect whether asparagine acts directly on RIG-I. We thus tested the effect of asparagine
277 on CBL-mediated ubiquitination of RIG-I in vitro. In the presence of E1, E2, ATP and
278 Ub, CBL promoted RIG-I ubiquitination, and asparagine addition strikingly enhanced
279 ubiquitination (Figure 5C). Notably, microscale thermophoresis (MST) assay, an in
280 vitro assay for direct interaction between proteins and small molecules, revealed that
281 asparagine had a high affinity to bind to RIG-I with a K_d of 303 μM (Figure 5D), but
282 did not show any affinity to CBL (Figure 5E). Thus, these results indicated that
283 asparagine could directly bind to RIG-I and promote its degradation. We further
284 observed that asparagine mediated reduction of the RIG-I and p-IRF3 (Figure 5F and
285 Supplemental Figure 7, E and F) as well as downregulation of IFN- β and CCL5 (Figure
286 5G and Supplemental Figure 7, G and H) were partially rescued by CBL knockdown.

287

288 Then, we detected the function of CBL knockdown on tumor growth and CD8⁺ T
289 cell infiltration. The results revealed that silencing of CBL partially rescued the
290 promotion of tumor growth and reduction of CD8⁺ T cells infiltration caused by

291 asparagine (Supplemental Figure 7, I-L). Furthermore, we found that loss of RIG-I
292 significantly increased the size of tumors derived from bladder cancer cells depleted
293 ASNS (Figure 5H). ASNS deficiency resulted in an obvious increase in infiltration of
294 CD8⁺ T cells, which was attenuated by RIG-I knockdown (Figure 5I). Taken together,
295 these data indicate that asparagine promotes the K48-linked ubiquitination of RIG-I by
296 CBL, thereby attenuating antitumor immune response.

297

298 **Asparagine restriction sensitizes tumors to PD-1 blockade**

299 Tumor mutation burden has been proposed as a predictive biomarker for response to
300 ICIs (42). Based on the high mutation profiles of bladder cancer, we therefore explored
301 the therapeutic effect of PD-1 blockade monotherapy in vivo. We found that PD-1
302 blockade alone had minimal effect on tumor growth delaying effect (Supplemental
303 Figure 8, A-D), consistent with previous report (43). Thus, it is necessary to improve
304 the efficacy of ICIs by developing combination therapies.

305

306 Considering that ASNS inhibition could enhance CD8⁺ T cells infiltration and
307 promote its activation, we further explored whether ASNS could affect the efficacy of
308 anti-PD-1 treatment preclinically. We conducted tumor growth experiments with anti-
309 PD-1 antibody in syngeneic mice inoculated with ASNS-deficient MB49 tumor cells.
310 Our results demonstrated that anti-PD-1 antibody synergized with ASNS deficiency in
311 suppressing tumor growth (Figure 6A). Flow cytometry analysis also showed that
312 ASNS knockdown combination with anti-PD-1 treatment significantly increased the
313 infiltration of CD8⁺ T cells (Figure 6B). More importantly, ASNase markedly enhanced
314 the antitumor effects of PD-1 blockade in the subcutaneous tumor models established
315 by MB49 cells (Figure 6, C-E). Further analysis of immune infiltration revealed that
316 combination treatment could also promote CD8⁺ T cells infiltration (Figure 6F). In
317 addition, there was no obvious difference in body weight among the four groups of
318 mice (Figure 6G). Consistent with the observations made in MB49 tumor mice, a
319 notable delay in tumor growth was observed in MBT2 tumor mice treated with the

320 ASNase and PD-1 blockade (Figure 6H and Supplemental Figure 8, E and F).
321 Furthermore, in terms of that the subcutaneous model does not faithfully recapitulate
322 the microenvironment of bladder cancer, we applied the orthotopic bladder tumor
323 model along with ASNase and anti-PD-1 treatment. As shown in Figure 6I-J, ASNase
324 alone reduced tumor growth, and the combination of anti-PD-1 and ASNase more
325 efficiently suppressed tumor progression. Immunofluorescence staining results
326 indicated that anti-PD-1 antibody increased CD8⁺ T cells number infiltrated in tumors,
327 which could be strengthened upon ASNase treatment (Figure 6J). Altogether, these
328 results indicate a potent synergy between ASNS inhibition and PD-1 blockade in
329 controlling tumor growth in bladder cancer.

330

331 **Upregulated ASNS leads to immunotherapy resistance in bladder cancer**

332 To further explore the profiles of ASNS in bladder cancer, we mined the TCGA dataset
333 and found that the mRNA level of ASNS was significantly upregulated in bladder
334 cancer (Figure 7A). We then confirmed that the level of ASNS protein was higher in
335 bladder cancer tissues than that in paired normal bladder tissues (Figure 7B). Moreover,
336 Immunohistochemical (IHC) staining in bladder cancer tissues array showing the
337 expression of ASNS was upregulated in tumor tissues (Figure 7C). Further Kaplan-
338 Meier analysis revealed that high expression of ASNS was associated with poor overall
339 survival for bladder cancer patients (Figure 7D). Next, we verified the correlation
340 between tumor ASNS, RIG-I, and CD8 expression in tissues of patients with cancer.
341 IHC staining exhibited a negative correlation between tumor CD8 expression and
342 ASNS expression in human bladder cancer clinical samples (Figure 7, E and F). Similar
343 to CD8, we found that tumor RIG-I expression was also inversely correlated with ASNS
344 protein expression (Supplemental Figure 9A). Furthermore, the infiltration degree of
345 CD8⁺ T cells showed a remarkable positive correlation with RIG-I (Supplemental
346 Figure 9B).

347

348 To further assess the clinical value of ASNS in ICIs therapy, we analyzed

349 immunotherapy cohort containing 57 bladder cancer patients treated with ICIs from our
350 hospital (301-immune cohort). The expression of ASNS at baseline was lower in
351 responders to ICIs compared with non-responders (Figure 7, G and H, and
352 Supplemental Figure 9C). Meanwhile, low levels of ASNS expression were associated
353 with improved progression-free survival in these patients (Figure 7I). Moreover, multi-
354 color IF images confirmed a negative correlation between ASNS expression and RIG-
355 I expression, CD8⁺ T cells infiltration (Figure 7J), revealing the mechanism of response
356 or non-response to ICIs treatment. Thus, these data indicated that ASNS could be a
357 predictive biomarker for bladder cancer ICIs therapy.

358

359 **Discussion**

360 Recently, ICIs therapy has become a promising therapeutic strategy with bladder cancer
361 due to its high levels of mutational burden (2). However, only a minority of patients
362 benefit from this strategy while a considerable proportion of patients either fail to
363 respond or progress rapidly to resistance after initial response (8). Therefore, finding
364 predictive biomarkers for increasing immune response and developing therapeutic
365 strategies to potentiate immunotherapy efficacy are urgently needed. Our study found
366 that ASNS expression is a predictive biomarker for immunotherapy response in bladder
367 cancer, and FDA-approved ASNase dramatically boosts the antitumor efficacy of anti-
368 PD-1 therapy. Anti-PD-1 therapy combined with ASNase in advanced bladder cancer
369 is worthy to investigate in future clinical trials. Previous studies showed that asparagine
370 availability favors tumor cell proliferation, metastasis and survival ability in various
371 types of cancers (27-29), while we found that knockdown of ASNS or asparagine
372 addition had no obvious effect on proliferation or migration of bladder cancer cells,
373 indicating cancer type-specific functions in asparagine metabolism. However, further
374 research should focus on the underlying mechanisms of ASNS upregulation in bladder
375 cancer, which may help to advance understanding its special role.

376

377 Modulation of amino acid metabolism has emerged as a way to reprogram the

378 tumor microenvironment and has shown great promise for cancer treatment, but major
379 studies have focused on immune cells themselves so far (20-22, 44, 45). As a
380 nonessential amino acid, asparagine uptake and biosynthesis enable CD8⁺ T cells
381 activation (early phase) (24-26), while exerting opposing effects during differentiation
382 (late phase) (26). These studies revealed asparagine as a critical metabolic node to shape
383 T cell effector functions and antitumor responses. However, it is unclear whether
384 asparagine has any effect on tumor-intrinsic functions to regulate immune responses.
385 Our data demonstrate that limiting asparagine by knockdown of ASNS or treatment
386 with ASNase in bladder cancer facilitates RIG-I mediated IFN-I signaling, promoting
387 the intratumoral CD8⁺ T cells infiltration and PD-1 blockade efficacy. Together, these
388 encouraging results imply that remodeling of asparagine metabolism is critical for
389 relieving tumor-mediated immunosuppression and effective way to enhance antitumor
390 immunity.

391

392 Increasing evidences indicate that the exclusion of CD8⁺ T cells in TME is
393 associated with poor response to immunotherapy (30, 31). Herein, we demonstrated
394 that knockdown of ASNS could potentiate recruitment and activation of CD8⁺ T cells
395 in bladder cancer. However, ASNS deficiency-mediated antitumor responses was not
396 completely reversed by CD8 depletion in syngeneic mice. In contrast, depletion of IFN-
397 β and anti-IFNAR1 antibody treatment almost completely reversed tumor regression
398 mediated by ASNS knockdown in syngeneic mice, suggesting that other types of
399 immune cells besides CD8⁺ T cells might also contribute to ASNS loss-triggered
400 antitumor immunity. Previous studies have shown that cytotoxic CD4⁺ T cells and NK
401 cells could mediate the antitumor responses of bladder cancer (46, 47). We
402 hypothesized that although silencing of ASNS showed no obvious difference in the
403 number of CD4⁺ T cells and NK cells in TME, it may alter their status and function.

404

405 Post-translational modification of the RLRs directly regulates their expression and
406 activity, subsequently modulating the downstream IFN-I signaling (48, 49). Of note,

407 K48-linked ubiquitylation catalyzed by several E3 ligases, such as RNF122, RNF125,
408 CBL or STUB1, contributes to the degradation of RIG-I, thereby influencing pathway
409 activation (41, 50-52). By far, little is known about whether nutrient metabolite is
410 crucially involved in the regulation of RIG-I-IFN signaling. In this study, we identify
411 asparagine as a metabolic regulator of RIG-I stability and verify that asparagine
412 directly binds to RIG-I, promoting CBL-mediated polyubiquitination and proteasomal
413 degradation of RIG-I. Previous studies report the metabolism-independent role for
414 asparagine in the direct modulation of LKB1 and LCK kinase activity (24, 29). We
415 uncover that asparagine could be an endogenous metabolite binding to RIG-I and
416 regulate its stability. However, further structural study may be required to
417 comprehensively understand how asparagine acts on RIG-I-CBL complex.

418

419 In conclusion, our study establishes a critical role of asparagine in limiting type I
420 IFN signaling and identifies RIG-I as a direct sensor of asparagine, which furnishes a
421 rationale for future clinical applications of the combinatorial use of ASNase and ICIs
422 in bladder cancer.

423

424 **Methods**

425 *Sex as a biological variable.* Male and female human bladder cancer samples were
426 analyzed. Male and female mice were used in all mouse studies. In this study, sex was
427 not considered as a biological variable.

428

429 *Animals.* Six- to eight-week-old C3H mice were purchased by Beijing Vital River
430 Laboratory Animal Technology Co., Ltd (Beijing, China). C57BL/6 mice and BALB/c
431 nude mice aged 6-8 weeks were purchased from GemPharmatech Co., Ltd (Nanjing,
432 China). All mice were maintained at room temperature with free access to food and
433 water with a 12-h light/dark cycle in a barrier facility.

434

435 *Cell lines and clinical samples.* The bladder cancer cell lines UMUC3 were

436 obtained from the ATCC. HEK293T cells were also purchased from the ATCC. The
437 murine malignant bladder cell lines MB49 and MBT2 were purchased from Meisen
438 CTCC (Zhe jiang, China). The UMUC3, MB49 and MBT2 cells were cultured in
439 DMEM (Procell, China). All the medium were supplemented with 10% FBS (Procell,
440 China), 1% penicillin and streptomycin (Procell, China). The condition of incubator
441 was set as 37°C with 5% CO₂. All cell lines were routinely confirmed negative for
442 *Mycoplasma* contamination. Resected human bladder cancer tissues and their
443 corresponding clinical information were acquired from the Department of Urology of
444 the Chinese PLA General Hospital. The histologic and pathologic type of all tissues
445 were confirmed by three experienced pathologists independently. For the 301-immune
446 cohort, a total of 57 bladder cancer patients receiving ICIs were included from Chinese
447 PLA General Hospital (301). ICIs treatment efficacy was inspected by at least 3
448 pathologists based on the Response Evaluation Criteria in Solid Tumors (RECIST). The
449 samples were obtained with written informed consent of all patients before the research
450 started.

451

452 *Plasmids construction and transfection.* Short hairpin RNA sequences against
453 mouse Asns, Rig-i, Mavs, c-Cbl and human ASNS were synthesized by Biomed
454 (Beijing, China), and were cloned into the pLKO.1 vector. Knockdown plasmid against
455 mouse Sting has been constructed in our previous study (53). The overexpression vector
456 of RIG-I was kindly gifted from Weina Zhang (Academy of Military Medical Sciences,
457 Beijing, China). The human RNF122, RNF125, STUB1 and CBL cDNA were
458 synthesized by Biomed, which were cloned into pCMV-HA vector to construct
459 overexpression plasmid. SgRNA sequence of Ifnb was synthesized by Biomed (Beijing,
460 China), and was cloned into the lentiCRISPR v2 vector. The lentiviral vectors were
461 transfected in HEK293T cells with the PAX2 and VSVG packaging plasmid. After 48
462 h or 72 h transfection, supernatants were collected and concentrated with Lentivirus
463 Concentration Reagent (GenStar, China) for overnight in 4°C. To construct the stably
464 transfected cell lines, cells were infected with relative lentiviruses for 24 h, then were

465 screened with puromycin for 1 weeks. shRNA sequences are also listed in Supplemental
466 Table1.

467

468 *Cell viability assays.* For the cell proliferation assay, the bladder cancer cells were
469 seeded in 96-well plates in 100 μ l complete culture media for various time periods
470 (2000 cells per well). Cell Counting Kit-8 assay (Dojindo, Japan) was performed to
471 measure cell viability according to the manufacturer's instructions.

472

473 *Animal experiments.* For the subcutaneous tumorigenesis experiments, 6- to 8-
474 week-old BALB/c nude mice, C57BL/6 and C3H mice were used. MB49 (5×10^5 per
475 mouse) and MBT2 (1×10^6 per mouse) cells stably transfected with the pLKO.1-
476 shAsns#1 plasmid or pLKO.1-Vector plasmid were subcutaneously injected into the
477 right flank of each mouse. When a tumor was palpable, it was measured using a caliper
478 every 3-4 days, and its volume was calculated according to the formula volume = length
479 \times width² \times 0.5. Four days after implantation, mice were treated with 100 μ g of either
480 control IgG2 α (Bioxcell, BE0085, USA) or anti-PD-1 antibody (Bioxcell, BE0146,
481 USA). The drugs were administered twice a week for 3 weeks. For Asparagine
482 experiment, mice were fed with drinking water containing with or without 10mM
483 Asparagine (Solarbio, China). For drug combination experiments, 5-week-old
484 C57BL/6 or C3H mice were inoculated subcutaneously with MB49 cells (5×10^5 per
485 mouse) or MBT2 cells (1×10^6 per mouse), respectively. Next, mice received treatment
486 i.p. with vehicle or ASNase (2 U per g) (ProSpec, Israel) three times a week for 3 weeks.
487 In addition, 100 μ g of anti-PD-1 antibody were injected on days 5 twice a week for 3
488 weeks in combination with the ASNase. For neutralization of IFNAR1, tumor-bearing
489 mice were injected i.p. with 200 μ g/mouse anti-IFNAR1 (BioXcell, BE0241, USA) at
490 on days 0, 7, 14 and 21.

491

492 *Quantitative real-time PCR.* Briefly, total RNA was isolated from bladder cancer
493 cells in each condition using FastPure Cell/Tissue Total RNA Isolation Kit V2 (Vazyme,

494 China) according to the manufacturer's instructions. RNA of each sample was
495 complementarily reversed to cDNA by HiScript III RT SuperMix for qPCR (Vazyme,
496 China). cDNA product of each sample was used as template to conduct quantitative
497 PCR by ChamQ Universal SYBR qPCR Master Mix (Vazyme, China). Quantitative
498 RT-PCR was performed using CFX96 Real-Time PCR System (Bio-Rad, USA). The
499 fold changes of gene expression were calculated after being normalized to 18s or ACTB.
500 The primer pairs used in this study were listed in Supplemental Table1.

501

502 *Western blotting analysis.* Briefly, cells were lysed by using RIPA buffer
503 containing proteinase inhibitors cocktail and PMSF on ice for 30 min. Protein samples
504 were quantified using BCA protein assay kit (Solarbio, China) and boiled in 5 × loading
505 buffer for 10 min at 95°C. Protein lysates were resolved by SDS-PAGE and transferred
506 onto polyvinylidene difluoride (PVDF) membrane. Then, the membranes were blocked by 5%
507 skimmed milk and probed with primary antibodies against Actin (bioeasytech, BE0033,
508 China), Asns (Proteintech, 14681-1-AP, USA), Sting (Proteintech, 19851-1-AP, USA),
509 Mavs (Proteintech, 14341-1-AP, USA), Rig-i (CST, 4200, USA), Mda5 (ABclonal,
510 A2419, China), Irf3 (CST, 4302, USA), p-Irf3 (CST, 29047, USA) and CBL
511 (Proteintech, 25818-1-AP, USA) at 4°C overnight. Membranes were washed with
512 TBST for three times and then incubated with HRP-conjugated anti-rabbit (Proteintech,
513 SA00001-2, USA) or anti-mouse (Proteintech, SA00001-1, USA) secondary antibodies
514 at room temperature for 1 h. Finally, the protein bands were visualized using ECL
515 substrate kit via QuickChemi 5200 Imaging System.

516

517 *Migration assays.* For migration assays, approximately 4×10^4 cells in 200 μ L
518 serum-free culture media were seeded in the upper chamber of 24-well Transwell
519 chamber system. About 600 μ L culture media with 10% FBS were added to the lower
520 chamber. After incubation for 24 h, cells were fixed in paraformaldehyde for 15 min
521 and then stained with 0.1% crystal violet for 30 min. The migrated cells were counted
522 in three randomly selected fields.

523 *FACS analysis with tumor-infiltrating immune cells.* Mice harboring tumors were
524 collected after inoculation, weighed, and mechanically minced and digested in DNase
525 I and collagenase IV (Sigma, USA) for 60 min at 37°C. The dissociated cells were
526 filtered by 70 µm cell strainers (BIOFIL, China) to obtain single cell suspension for
527 flow cytometry analysis. Tumor cells were washed with RPMI-1640 medium and lysed
528 with RBC Lysis Solution (Beyotime, China). Then, BV510 anti-mouse CD45
529 (BioLegend, 103137, USA), BV605 anti-mouse CD3 (BioLegend, 100237, USA),
530 Alexa Fluor® 488 anti-mouse CD4 (BioLegend, 100423, USA), APC/Fire™ 750 anti-
531 mouse CD8a (BioLegend, 100766, USA) and APC-mouse NK1.1 (BioLegend, 108710,
532 USA) were used to stain cell members for 30 min in the dark. Flow cytometer was
533 applied to detect stained cells, and FlowJo software was used to analyze the data.

534

535 For cytokine staining, tumor cells are digested into single cell suspension and
536 centrifuged for 5 min at 1500 rpm. All cells were then cultured in 1640 medium (RPMI-
537 1640 with 10% FBS and penicillin/streptomycin) with GolgiPlug (BD, 554724, USA)
538 and eBioscience™ (Thermo Fisher Scientific, 00-4970-93, USA) for 3 h at 37 °C. Cells
539 were washed and live/dead staining (Thermo Fisher Scientific, 65-0865-14) and BV421
540 anti-mouse CD45 (BioLegend, 103133, USA) and PerCP anti-mouse CD8 (BioLegend,
541 100731, USA) staining were performed. Then cells were fixed for 1 h at room
542 temperature in Fixation/ Permeabilization Concentrate and washed in permeabilization
543 buffer (Thermo Fisher Scientific, 00-5523-00, USA). APC anti-mouse TNFα
544 (BioLegend, 506307, USA) and PE anti-mouse IFNγ (BD, 554412, USA) staining was
545 performed in permeabilization buffer at room temperature for 30 mins. Cells were
546 washed and resuspended in FACS buffer for analysis on flow cytometer.

547

548 *Immunohistochemical staining.* Paraffin-embedded tissues were sectioned and
549 used to detect the expression of ASNS, RIG-I and CD8. IHC staining was conducted as
550 described previously. Briefly, samples were incubated with primary antibodies,
551 including anti-ASNS (proteintech, 14681-1-AP, USA), anti-RIG-I (ABclonal, A21421,

552 China) and anti-mCD8a (CST, 98941, USA) at 4°C overnight. Sections were incubated
553 with enzyme-conjugated secondary antibody followed by washing three times with
554 PBS. After washing, sections were incubated with DAB substrate kit. Sections were
555 counterstained with hematoxylin. The stained bladder cancer tissues were scored based
556 on a scoring method as follows: staining intensity was scored 0 (negative), 1 (low), 2
557 (moderate), and 3 (high). Staining range was scored 0 (0% stained), 1 (1%-25% stained),
558 2 (26%-50% stained), and 3 (51%- 100% stained). The total score was calculated
559 according to the formula score = intensity score × percentage score.

560

561 *Immunofluorescence.* For dsRNAs immunofluorescence, cells were plated on
562 glass coverslips in 24-well. After overnight cultivation, cells were washed three times
563 with PBS and then fixed with 4% formaldehyde at room temperature for 20 minutes
564 and permeabilized with 0.5% Triton-X100 in PBS for 5 minutes at room temperature.
565 Then, cells were blocked by 1% BSA and incubated in the J2 antibody (SCICONS,
566 10010200, Hungary) at 4°C overnight. The following day, cells were washed three
567 times with PBST and incubated with ABflo® 594-conjugated Goat anti-Mouse IgG
568 (ABclonal, AS054, China) for 1 h at room temperature, followed sealing with antifade
569 mounting medium containing DAPI.

570

571 For multiplex immunofluorescence staining of tissues, tumors were captured and
572 fixed in 10% formalin overnight and embedded in paraffin. The embedded tissues were
573 sectioned into slices with a thickness of 4 μm, deparaffinized and hydrated, antigen
574 retrieved in 10 mmol/L sodium citrate for 20 mins in a microwave oven and cooling to
575 room temperature slowly. Sections were permeabilized with 0.5% Triton X-100 in PBS
576 for 5 mins and then blocked with 2% BSA in PBS for 1 h at room temperature. The
577 sections were incubated with anti-mCD8a (CST, 98941, USA), anti-GZMB
578 (proteintech, 13588-1-AP, USA), anti-hCD8a (CST, 70306, USA), ASNS (proteintech,
579 14681-1-AP, USA) and anti-RIG-I (ABclonal, A21421, China) overnight at 4°C.
580 Subsequently, sections were washed with PBS and incubated with fluorescein-

581 conjugated secondary antibody at room temperature for 1 h. After incubation with
582 DAPI, the slides were imaged and visualized using CLSM 600 confocal laser scanning
583 microscope (Sunnysoptop, China).

584

585 *In vivo experiments with CD8 depletion.* MB49 (5×10^5 per mouse) and MBT2
586 (1×10^6 per mouse) cells stably transfected with the pLKO.1-shAsns#1 plasmid,
587 pLKO.1-shAsns#2 plasmid or pLKO.1-Vector plasmid were subcutaneously injected
588 into 6- to 8-week-old C57BL/6 mice and C3H mice, respectively. To evaluate the role
589 of CD8⁺ T cells in mice, the 200 μ g of anti-CD8a antibody (MCE, HY-P99129, USA)
590 was injected intraperitoneally on days -3, 0, 3, 8 and 11. Equal amounts of IgG isotype
591 antibodies were injected as a control. Tumor volume and growth curve were detected
592 as mentioned above.

593

594 *RNA-seq and Gene Set Enrichment Analysis (GSEA).* Total RNA isolated using
595 FastPure Cell/Tissue Total RNA Isolation Kit V2 (Vazyme, China). RNA-seq analysis
596 was performed by Majorbio Bio-pharm Technology Co., Ltd (Shanghai, China).
597 Transcriptome library was prepared following TruSeq RNA sample preparation Kit
598 from Illumina (San Diego, CA) using 1 μ g of total RNA. DEGs with $|\log_2FC| > 1.5$ and
599 P adjust value ≤ 0.05 were considered to be significantly different expressed genes. The
600 data were analyzed on the online platform of Majorbio Cloud Platform. Sequencing
601 results were deposited in the Gene Expression Omnibus database (GSE270353) with
602 accession number ejsjswsgdhupzqj. GSEA algorithm was used to analyze the biological
603 functions of the genes based on type I IFN-related molecular signatures collected from
604 Molecular Signatures Database (MSigDB).

605

606 *Luminex liquid suspension biochip detection.* MBT2 cells stably transfected with
607 the pLKO.1-shAsns#1 plasmid or pLKO.1-Vector plasmid were cultured in the 6-well
608 plates. After 24 h, cell culture supernatants were collected, and the inflammatory
609 cytokines and chemokines were detected (including: CCL1, CCL2, CCL3, CCL4,

610 CCL5, CCL7, CCL11, CCL12, CCL17, CCL19, CCL20, CCL22, CCL24, CCL27,
611 CXCL1, CXCL5, CXCL10, CXCL11, CXCL12, CXCL13, CXCL16, CX3CL1, IL-2,
612 IL-4, IL-6, IL-10, IL-16, GM-CSF, IFN- γ , IL-1 β , TNF- α) by a Luminex protein
613 biochip testing system (Wayen Biotechnologies, Shanghai, China) according to
614 manufacturer's instruction. The data were measured and collected by the Luminex 200
615 system. The results were showed in supplemental Table2.

616

617 *ELISA.* Cell culture supernatants were collected from 6-well plates, and the
618 presence of the cytokine/chemokine proteins was determined using the Mouse IFN- β
619 and Mouse CCL5 ELISA kit (Elabscience, USA) according to the manufacturer's
620 instructions. The concentrations of different cytokine/chemokine proteins were
621 calculated based on OD values at a detection wavelength of 450 nm.

622

623 *Co-IP.* HEK293T cells were transfected with Flag-RIG-I and HA-RNF122, HA-
624 RNF125, HA-STUB1 and HA-CBL together with Asparagine (Solarbio, China) for 42
625 h and cultured in medium containing MG132 (MCE, USA) for a further 6 h before co-
626 immunoprecipitation. Then the cells were lysed with NP-40 buffer plus complete
627 protease inhibitors PMSF and cocktail, and samples were cleaved on ice for 30 min.
628 The lysates were centrifuged at 12,000 rpm for 10 min at 4°C. About 5-10% of the
629 supernatants were used as input group, and the remaining samples were divided equally
630 into IgG group and Flag group. The protein A/G beads were added in IgG or Flag
631 antibodies at 4°C for 2h. Then the supernatants were incubated with antibodies-beads
632 mix at 4°C overnight. Proteins interacting with beads were eluted off by re-suspending
633 the beads in 1 \times SDS-PAGE loading buffer followed by heating at 95°C for 10 min.
634 Proteins were separated by SDS-PAGE, followed by immunoblotting analysis with the
635 Flag (proteintech, 66008-4-Ig, USA), HA (proteintech, 51064-2-AP, USA) and Ub-K48
636 (ABclonal, A3606, China) antibodies.

637

638 *In vitro ubiquitination assay.* Flag-RIG-I and HA-CBL were expressed in

639 HEK293T cells and purified using Flag and HA beads, respectively. The reaction was
640 carried out at 37 °C for 2 h in 20 µl reaction buffer (40 mM Tris-HCl at pH 7.6, 2.5 mM
641 Mg²⁺-ATP, 2 mM dithiothreitol) containing the following components: 50 µM of
642 ubiquitin, 100 nM E1, 1 µM E2, 2 µM HA-CBL, 5 µM Flag-RIG-I. The samples were
643 stopped by adding SDS and boiled for 10 min, and then resolved by SDS-PAGE
644 followed by immunoblot analysis using a monoclonal anti-Ub antibody.

645

646 *Microscale thermophoresis (MST) assay.* MST is a biomolecular interaction
647 analysis technology that measures the affinity between a ligand and a target molecule
648 (54). Briefly, the HEK293T cell lysate was collected after 48 h transfection with the
649 Flag-RIG-I or HA-CBL plasmid. We purified Flag-tagged RIG-I and HA-tagged CBL
650 by acid elution method. In total, 16 titration series of asparagine were prepared
651 beginning at a concentration of 5mM and mixed with purified protein. All the samples
652 were loaded into MST NT.115 standard glass capillaries and measurement was carried
653 out using the MO. Control software.

654

655 *Orthotopic bladder tumor model.* An orthotopic bladder tumor mouse model was
656 established as described previously (55) with minor modifications. In brief, under
657 anesthesia, the C57BL/6 mice were placed in a supine position on a thermostatic
658 blanket. Then, a 1-cm midline incision through the skin of the abdominopelvic region
659 was made to locate the urinary bladder. Luc-labeling MB49 cells were resuspended
660 with 50% Matrigel (Lablead, China) mixed with PBS (5×10^3 cells per mouse) and
661 were injected into the bladder wall of mice using insulin syringe. The bladder was
662 placed back inside while ensuring that all other organs were in their proper position.
663 Mice were left for at least 5 days for tumor development. After tumor volume was
664 measured by living image, mice were randomly allocated into four groups for ASNase
665 or anti-PD-1 treatment. For bioluminescent imaging, mice were given 200 µL (15mg/ml)
666 D-luciferin potassium salt (Lablead, China) intraperitoneally and imaged on a live
667 imaging system (Berthold LB983, Germany).

668 *Statistics.* The results are presented as the mean \pm SD. Kaplan-Meier method and
669 log-rank test were used to calculate overall survival rates. The significance of
670 intergroup differences was determined with 2-tailed Student's t-test, 1-way ANOVA or
671 2-way ANOVA. Statistical significance was assessed using GraphPad Prism software.
672 A difference of $P < 0.05$ was considered statistically significant. *, $P < 0.05$; **, $P <$
673 0.01 ; and ***, $P < 0.005$ were defined.

674

675 *Study approval.* All bladder cancer tissue samples used in this study were obtained
676 from patients with their informed consent, and the use of these samples was approved
677 by the Institutional review board of the Chinese PLA General Hospital. All animal
678 experiments were performed in accordance with institutional regulations and approval
679 by the Institutional Animal Care and Use Committee of the Chinese PLA General
680 Hospital.

681

682 *Data availability.* RNA-Seq data reported in this paper were deposited in the Gene
683 Expression Omnibus (GEO) database (GSE270353) with accession number
684 ejsjswsgdhupzqj. Values for all data points in graphs are reported in the Supporting
685 Data Values file. All unique/stable reagents generated in this study are available from
686 the corresponding author with a completed material transfer agreement.

687

688 **Authors' Contributions**

689 **W. Wei:** Conceptualization, data curation, formal analysis, investigation, methodology,
690 writing-original draft. **H. Li:** Investigation, methodology. **S. Tian:** Formal analysis,
691 validation, methodology. **C. Zhang:** Formal analysis, investigation. **J. Liu:** Formal
692 analysis, investigation. **W. Tao:** Formal analysis, investigation. **T. Cai:** Investigation.
693 **Y. Dong:** Investigation. **C. Wang:** Formal analysis. **D. Lu:** Investigation. **Y. Ai:**
694 Resources. **W. Zhang:** Resources. **H. Wang:** Resources. **K. Liu:** Conceptualization,
695 data curation. **Y. Fan:** Data curation. **Y. Gao:** Conceptualization, data curation, funding
696 acquisition. **Q. Huang:** Conceptualization, data curation, funding acquisition. **X. Ma:**

697 Data curation, visualization. **B. Wang:** Conceptualization, data curation, funding
698 acquisition. **X. Zhang:** Conceptualization, resources, supervision, funding acquisition.
699 **Y. Huang:** Conceptualization, resources, data curation, formal analysis, supervision,
700 funding acquisition, writing-original draft.

701

702 **Acknowledgements**

703 We thank Prof. Xin Pan and Prof. Weina Zhang for helpful discussions and advice for
704 this project. We sincerely thank all patients in the study. We thank the Wayen
705 Biotechnologies (Shanghai, China) for providing Luminex services. We also thank the
706 Majorbio Company (Shanghai, China) for their enthusiastic support of this RNA-seq
707 analysis. This study was supported by the grants from the National Natural Science
708 Foundation of China (82103594 to Y. Huang, 82273412 to Q. Huang and 82372704 to
709 B. Wang.), the National key research and development program (2022YFB4701700 to
710 Y. Gao), the Youth Fund of Chinese PLA General Hospital (22QNCZ022 to Y. Huang)
711 and the Minimally Invasive Innovation Team of the Urology Department of the Chinese
712 PLA General Hospital (X. Zhang).

713

714 **References**

- 715 1. Sanli O, et al. Bladder cancer. *Nat Rev Dis Primers*. 2017;3:17022.
- 716 2. Alifrangis C, et al. Molecular and histopathology directed therapy for advanced bladder cancer.
717 *Nat Rev Urol*. 2019;16(8):465-83.
- 718 3. Antoni S, et al. Bladder Cancer Incidence and Mortality: A Global Overview and Recent Trends.
719 *Eur Urol*. 2017;71(1):96-108.
- 720 4. Patel VG, et al. Treatment of muscle-invasive and advanced bladder cancer in 2020. *CA Cancer*
721 *J Clin*. 2020;70(5):404-23.
- 722 5. Patel MR, et al. Avelumab in metastatic urothelial carcinoma after platinum failure (JAVELIN
723 Solid Tumor): pooled results from two expansion cohorts of an open-label, phase 1 trial. *Lancet*
724 *Oncol*. 2018;19(1):51-64.
- 725 6. Sharma P, et al. Nivolumab in metastatic urothelial carcinoma after platinum therapy
726 (CheckMate 275): a multicentre, single-arm, phase 2 trial. *Lancet Oncol*. 2017;18(3):312-22.
- 727 7. Felsenstein KM, and Theodorescu D. Precision medicine for urothelial bladder cancer: update
728 on tumour genomics and immunotherapy. *Nat Rev Urol*. 2018;15(2):92-111.
- 729 8. Schneider AK, et al. The multifaceted immune regulation of bladder cancer. *Nat Rev Urol*.
730 2019;16(10):613-30.
- 731 9. Park J, et al. Microenvironment-driven metabolic adaptations guiding CD8(+) T cell anti-tumor

- immunity. *Immunity*. 2023;56(1):32-42.
- 733 10. Chen DS, and Mellman I. Elements of cancer immunity and the cancer-immune set point.
734 *Nature*. 2017;541(7637):321-30.
- 735 11. Schenkel JM, and Pauken KE. Localization, tissue biology and T cell state - implications for
736 cancer immunotherapy. *Nat Rev Immunol*. 2023;23(12):807-23.
- 737 12. Chen Y, et al. CD8(+) T cell-based cancer immunotherapy. *J Transl Med*. 2024;22(1):394.
- 738 13. Gebhardt T, et al. Stem-like exhausted and memory CD8(+) T cells in cancer. *Nat Rev Cancer*.
739 2023;23(11):780-98.
- 740 14. Corrales L, et al. Innate immune signaling and regulation in cancer immunotherapy. *Cell Res*.
741 2017;27(1):96-108.
- 742 15. Yu R, et al. Type I interferon-mediated tumor immunity and its role in immunotherapy. *Cell Mol*
743 *Life Sci*. 2022;79(3):191.
- 744 16. Heidegger S, et al. RIG-I activating immunostimulatory RNA boosts the efficacy of anticancer
745 vaccines and synergizes with immune checkpoint blockade. *EBioMedicine*. 2019;41:146-55.
- 746 17. Gstalder C, et al. Inactivation of Fbxw7 Impairs dsRNA Sensing and Confers Resistance to PD-
747 1 Blockade. *Cancer Discov*. 2020;10(9):1296-311.
- 748 18. Jiang Y, et al. Exploiting RIG-I-like receptor pathway for cancer immunotherapy. *J Hematol*
749 *Oncol*. 2023;16(1):8.
- 750 19. Rehwinkel J, and Gack MU. RIG-I-like receptors: their regulation and roles in RNA sensing.
751 *Nat Rev Immunol*. 2020;20(9):537-51.
- 752 20. Lemos H, et al. Immune control by amino acid catabolism during tumorigenesis and therapy.
753 *Nat Rev Cancer*. 2019;19(3):162-75.
- 754 21. Yang L, et al. Amino acid metabolism in immune cells: essential regulators of the effector
755 functions, and promising opportunities to enhance cancer immunotherapy. *J Hematol Oncol*.
756 2023;16(1):59.
- 757 22. Wang W, and Zou W. Amino Acids and Their Transporters in T Cell Immunity and Cancer
758 Therapy. *Mol Cell*. 2020;80(3):384-95.
- 759 23. Richards NG, and Kilberg MS. Asparagine synthetase chemotherapy. *Annu Rev Biochem*.
760 2006;75:629-54.
- 761 24. Wu J, et al. Asparagine enhances LCK signalling to potentiate CD8(+) T-cell activation and
762 anti-tumour responses. *Nat Cell Biol*. 2021;23(1):75-86.
- 763 25. Hope HC, et al. Coordination of asparagine uptake and asparagine synthetase expression
764 modulates CD8+ T cell activation. *JCI Insight*. 2021;6(9).
- 765 26. Gnanaprakasam JNR, et al. Asparagine restriction enhances CD8(+) T cell metabolic fitness and
766 antitumoral functionality through an NRF2-dependent stress response. *Nat Metab*.
767 2023;5(8):1423-39.
- 768 27. Gwinn DM, et al. Oncogenic KRAS Regulates Amino Acid Homeostasis and Asparagine
769 Biosynthesis via ATF4 and Alters Sensitivity to L-Asparaginase. *Cancer Cell*. 2018;33(1):91-
770 107.e6.
- 771 28. Knott SRV, et al. Asparagine bioavailability governs metastasis in a model of breast cancer.
772 *Nature*. 2018;554(7692):378-81.
- 773 29. Deng L, et al. p53-mediated control of aspartate-asparagine homeostasis dictates LKB1 activity
774 and modulates cell survival. *Nat Commun*. 2020;11(1):1755.
- 775 30. Joyce JA, and Fearon DT. T cell exclusion, immune privilege, and the tumor microenvironment.

- 776 *Science*. 2015;348(6230):74-80.
- 777 31. Park HR, et al. Angiopoietin-2-Dependent Spatial Vascular Destabilization Promotes T-cell
778 Exclusion and Limits Immunotherapy in Melanoma. *Cancer Res*. 2023;83(12):1968-83.
- 779 32. Dangaj D, et al. Cooperation between Constitutive and Inducible Chemokines Enables T Cell
780 Engraftment and Immune Attack in Solid Tumors. *Cancer Cell*. 2019;35(6):885-900.e10.
- 781 33. Zhao B, et al. Structural basis for concerted recruitment and activation of IRF-3 by innate
782 immune adaptor proteins. *Proc Natl Acad Sci U S A*. 2016;113(24):E3403-12.
- 783 34. Zhuang Q, et al. RNA Methyltransferase FTSJ3 Regulates the Type I Interferon Pathway to
784 Promote Hepatocellular Carcinoma Immune Evasion. *Cancer Res*. 2024;84(3):405-18.
- 785 35. Kato H, et al. Differential roles of MDA5 and RIG-I helicases in the recognition of RNA viruses.
786 *Nature*. 2006;441(7089):101-5.
- 787 36. Watanabe A, et al. Association of aberrant ASNS imprinting with asparaginase sensitivity and
788 chromosomal abnormality in childhood BCP-ALL. *Blood*. 2020;136(20):2319-33.
- 789 37. Uggenti C, et al. Self-Awareness: Nucleic Acid-Driven Inflammation and the Type I
790 Interferonopathies. *Annu Rev Immunol*. 2019;37:247-67.
- 791 38. Hur S. Double-Stranded RNA Sensors and Modulators in Innate Immunity. *Annu Rev Immunol*.
792 2019;37:349-75.
- 793 39. Takeuchi O, and Akira S. Pattern recognition receptors and inflammation. *Cell*.
794 2010;140(6):805-20.
- 795 40. Goubau D, et al. Cytosolic sensing of viruses. *Immunity*. 2013;38(5):855-69.
- 796 41. Chen W, et al. Induction of Siglec-G by RNA viruses inhibits the innate immune response by
797 promoting RIG-I degradation. *Cell*. 2013;152(3):467-78.
- 798 42. McGrail DJ, et al. High tumor mutation burden fails to predict immune checkpoint blockade
799 response across all cancer types. *Ann Oncol*. 2021;32(5):661-72.
- 800 43. Nadal R, et al. Progress in systemic therapy for advanced-stage urothelial carcinoma. *Nat Rev*
801 *Clin Oncol*. 2024;21(1):8-27.
- 802 44. Yuan H, et al. Lysine catabolism reprograms tumour immunity through histone crotonylation.
803 *Nature*. 2023;617(7962):818-26.
- 804 45. Fang L, et al. Methionine restriction promotes cGAS activation and chromatin untethering
805 through demethylation to enhance antitumor immunity. *Cancer Cell*. 2023;41(6):1118-33.e12.
- 806 46. Oh DY, et al. Intratumoral CD4(+) T Cells Mediate Anti-tumor Cytotoxicity in Human Bladder
807 Cancer. *Cell*. 2020;181(7):1612-25.e13.
- 808 47. Wong JKM, et al. TGF- β signalling limits effector function capacity of NK cell anti-tumour
809 immunity in human bladder cancer. *EBioMedicine*. 2024;104:105176.
- 810 48. Du G, et al. Retinoic acid-inducible gene-I like receptor pathway in cancer: modification and
811 treatment. *Front Immunol*. 2023;14:1227041.
- 812 49. Xu XX, et al. RIG-I: a multifunctional protein beyond a pattern recognition receptor. *Protein*
813 *Cell*. 2018;9(3):246-53.
- 814 50. Zhou P, et al. MLL5 suppresses antiviral innate immune response by facilitating STUB1-
815 mediated RIG-I degradation. *Nat Commun*. 2018;9(1):1243.
- 816 51. Arimoto K, et al. Negative regulation of the RIG-I signaling by the ubiquitin ligase RNF125.
817 *Proc Natl Acad Sci U S A*. 2007;104(18):7500-5.
- 818 52. Wang W, et al. RNF122 suppresses antiviral type I interferon production by targeting RIG-I
819 CARDS to mediate RIG-I degradation. *Proc Natl Acad Sci U S A*. 2016;113(34):9581-6.

820 53. Wu S, et al. Targeting STING elicits GSDMD-dependent pyroptosis and boosts anti-tumor
821 immunity in renal cell carcinoma. *Oncogene*. 2024;43(20):1534-48.
822 54. Wan J, et al. Astragaloside IV derivative HHQ16 ameliorates infarction-induced hypertrophy
823 and heart failure through degradation of lncRNA4012/9456. *Signal Transduct Target Ther*.
824 2023;8(1):414.
825 55. Wang M, et al. Acquired semi-squamization during chemotherapy suggests differentiation as
826 a therapeutic strategy for bladder cancer. *Cancer Cell*. 2022;40(9):1044-59.e8.

827

828

829

830

831

832

833

834

835

836

837

838

839

840

841

842

843

844

845

846

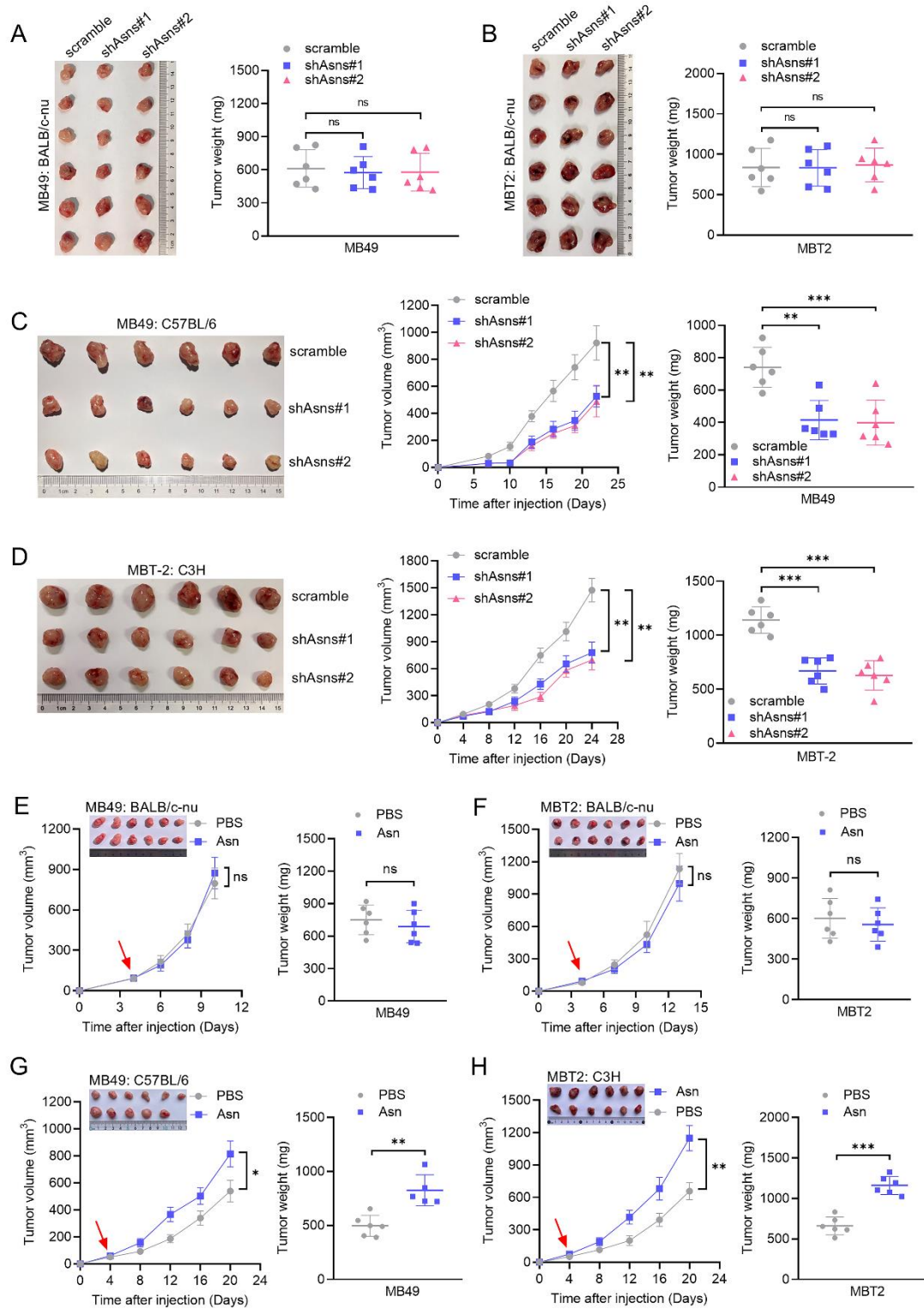
847

848

849

850

851



853

854 **Figure 1. Asparagine restriction attenuates tumor growth in syngeneic mice.**

855 (A) Tumor image and tumor weight of immunodeficient nude mice (n = 6) injected

856 subcutaneously with scramble or shAsns MB49 cells.

857 **(B)** Tumor image and tumor weight of immunodeficient nude mice (n = 6) injected
858 subcutaneously with scramble or shAsns MBT2 cells.

859 **(C)** Tumor growth curves and tumor weight of immunocompetent C57BL/6 mice (n =
860 6) injected subcutaneously with scramble or shAsns MB49 cells.

861 **(D)** Tumor growth curves and tumor weight of immunocompetent C3H mice (n = 6)
862 injected subcutaneously with scramble or shAsns MBT2 cells.

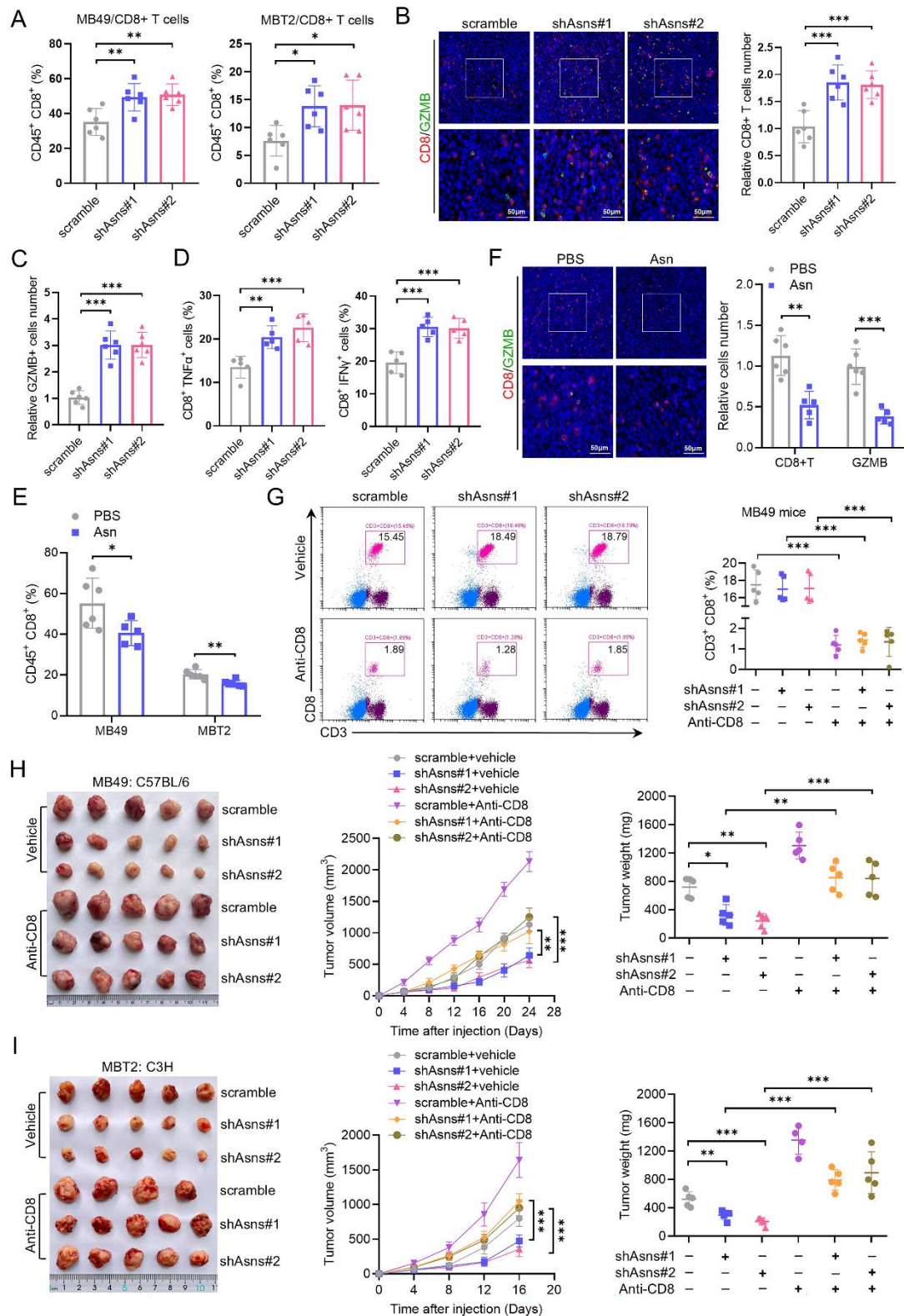
863 **(E)** Tumor growth curves and tumor weight of immunodeficient nude mice (n = 6)
864 injected subcutaneously with MB49 cells administrated with PBS or Asn.

865 **(F)** Tumor growth curves and tumor weight of immunodeficient nude mice (n = 6)
866 injected subcutaneously with MBT2 cells administrated with PBS or Asn.

867 **(G)** Tumor growth curves and tumor weight of immunocompetent C57BL/6 mice (n =
868 6) injected subcutaneously MB49 cells administrated with PBS or Asn.

869 **(H)** Tumor growth curves and tumor weight of immunocompetent C3H mice (n = 6)
870 injected subcutaneously MBT2 cells administrated with PBS or Asn.

871 Data were mean \pm SD. Statistical significance was calculated by two tailed unpaired
872 Student's t-tests for E, F, G and H. One-way ANOVA for A, B, C and D. ns, not
873 significant. **p<0.01, ***p<0.001.



874

875 **Figure 2. Knockdown of ASNS potentiates antitumor function of CD8+ T cells.**

876 (A) Tumor infiltrating CD8+ T cells from transplanted shAsns-MB49 tumors (n = 6) in

877 C57BL/6 mice and shAsns-MBT2 tumors (n = 6) in C3H mice were analyzed by flow

878 cytometry.

879 **(B-C)** Representative images and quantification of immunofluorescence for CD8 **(B)**
880 and GZMB **(C)** in scramble and shAsns-MB49 tumors (n = 6). Scale bars, 50 μ m.

881 **(D)** Flow staining and frequency of CD8+TNF α + and CD8+IFN γ + cells in shAsns-
882 MB49 and control tumors (n = 5).

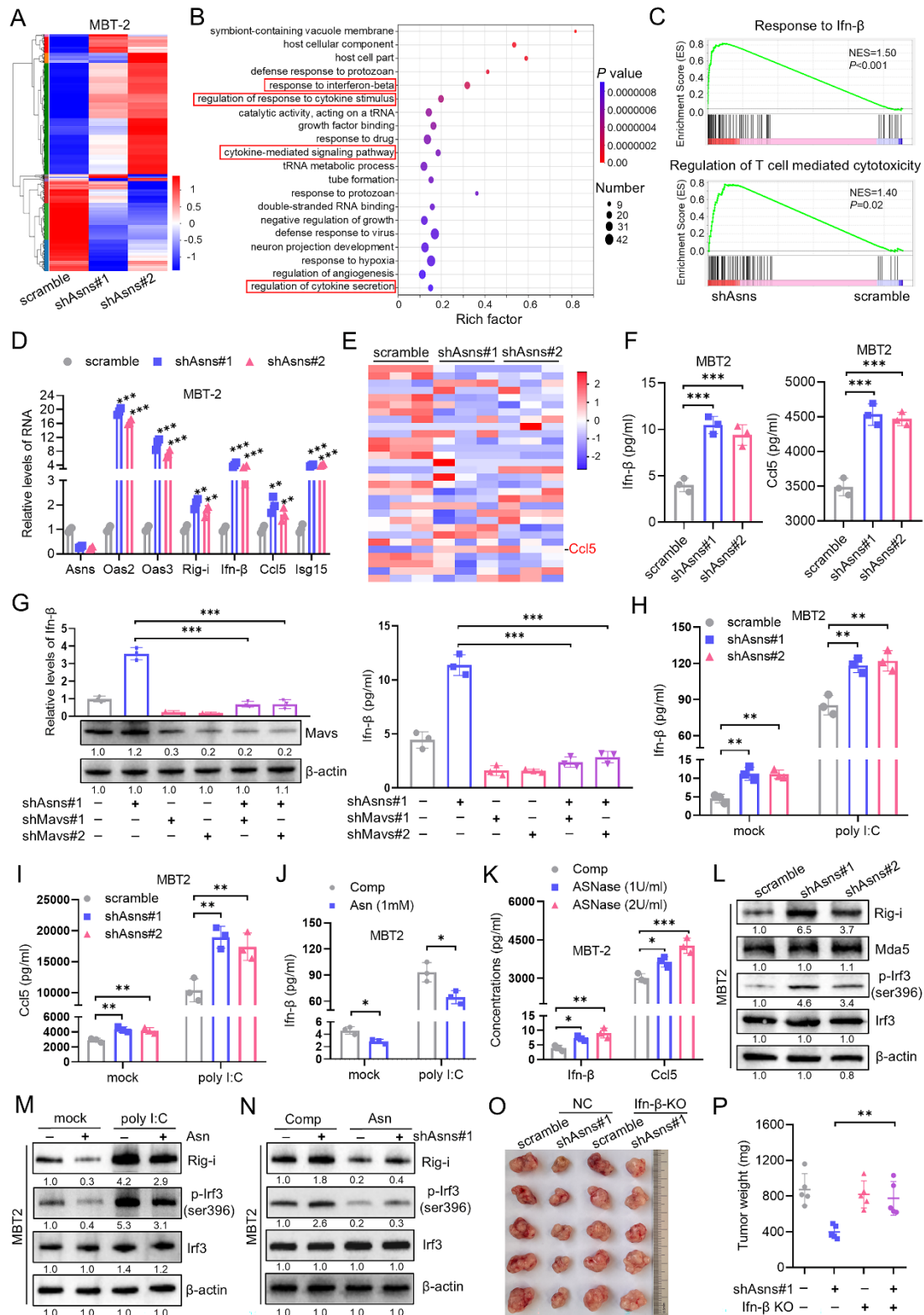
883 **(E)** Tumor infiltrating CD8+ T cells were analyzed by flow cytometry from
884 transplanted MB49 and MBT2 tumors (n = 6) in syngeneic mice administrated with
885 PBS or Asn.

886 **(F)** Representative images and quantification of immunofluorescence for CD8 and
887 GZMB in MB49 tumors administrated with PBS or Asn (n = 6). Scale bars, 50 μ m.

888 **(G)** C57BL/6 mice were subcutaneously inoculated with MB49 tumor cells and treated
889 with anti-CD8 antibody. Flow cytometry analysis of CD8+ T cells content in peripheral
890 blood of mice (n = 5) at the end of experiment.

891 **(H)** Tumor growth curves and tumor weight from scramble and shAsns-MB49 tumor
892 cells in C57BL/6 mice (n = 5) followed by intraperitoneal injection with anti-CD8
893 antibody.

894 **(I)** Tumor growth curves and tumor weight from scramble and shAsns-MBT2 tumor
895 cells in C3H mice (n = 5) followed by intraperitoneal injection with anti-CD8 antibody.
896 Data were mean \pm SD. Statistical significance was calculated by two tailed unpaired
897 Student's t-tests for E and F. One-way ANOVA for A, B, C and D. Two-way ANOVA
898 for G, H and I. *p<0.05, **p<0.01, ***p<0.001.



899

900 **Figure 3. Silencing of ASNS activates RIG-I-induced type I IFN signaling.**

901 (A) Heat map depicted the differentially expressed mRNA in the indicated MBT2 cells.

902 (B) Enrichment analysis for representative GO pathways in shAsns-mediated target

903 genes.

904 (C) GSEA plots of individual pathways enriched in shAsns-deficient MBT2 cells.

905 (D) qRT-PCR showed the relative expression levels of ISGs genes in the indicated

906 MBT2 cells.

907 (E) Heatmap of multiple cytokines and chemokines detected by Luminex protein

908 biochip testing system between Asns knockdown and the control groups in MBT2 cells

909 culture supernatants.

910 (F) ELISA experiment revealed the expression levels of Ifn- β and Ccl5 in culture

911 supernatants of the indicated MBT2 cells.

912 (G) qRT-PCR (left) and ELISA (right) assays showed the expression levels of Ifn- β in

913 the indicated MBT2 cells. Western blot analysis of cell lysates from the indicated MBT2

914 cells.

915 (H-I) Scramble or shAsns MBT2 cells were transfected with poly (I:C) (2 μ g/ml) for 8

916 h and the protein levels of Ifn- β (H) and Ccl5 (I) were determined by ELISA.

917 (J) ELISA assay showed the expression levels of Ifn- β protein in the indicated MBT2

918 cells.

919 (K) ELISA assay showed the expression levels of Ifn- β and Ccl5 in MBT2 cells treated

920 with ASNase for 48 h.

921 (L) Western blot analysis of cell lysates from the MBT2 cells stably transfected with

922 scramble and shAsns.

923 (M) Western blot analysis of cell lysates from the indicated MBT2 cells.

924 (N) Western blot analysis of cell lysates from the indicated MBT2 cells.

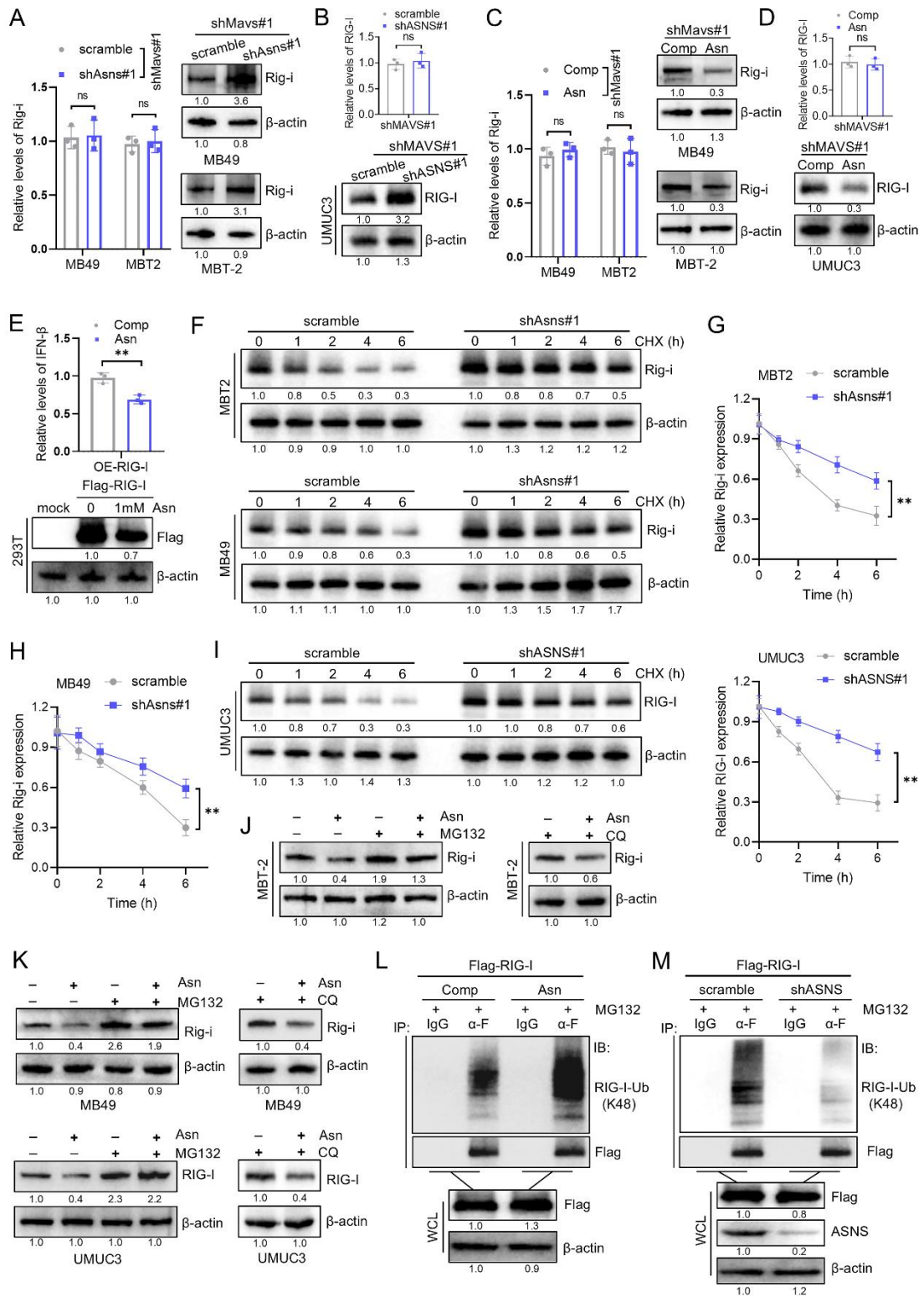
925 (O-P) Tumor image and tumor weight of immunocompetent C57BL/6 mice (n = 5)

926 injected subcutaneously with indicated MB49 cells.

927 Data were mean \pm SD. Statistical significance was calculated by two tailed unpaired

928 Student's t-tests for J. One-way ANOVA for D, F, H, I and K. Two-way ANOVA for G

929 and P. *p<0.05, **p<0.01, ***p<0.001.



930

931 **Figure 4. Asparagine facilitates the ubiquitination degradation of RIG-I.**

932 (A) qRT-PCR and western blot showed the expression levels of RIG-I mRNA and

933 protein in the indicated Murine bladder cancer cells.

934 **(B)** qRT-PCR and western blot showed the expression levels of RIG-I mRNA and
935 protein in the indicated UMUC3 cells.

936 **(C)** qRT-PCR and western blot showed the expression levels of Rig-i mRNA and
937 protein in the indicated Murine bladder cancer cells.

938 **(D)** qRT-PCR and western blot showed the expression levels of RIG-I mRNA and
939 protein in the indicated UMUC3 cells.

940 **(E)** qRT-PCR showed the expression levels of IFN- β in RIG-I-overexpressed HEK293T
941 cells cultured in complete medium (Comp) and medium added Asn (1mM) for 48 h.
942 Western blot showed the levels of RIG-I protein in the indicated groups.

943 **(F-H)** Western blot revealed the degradation kinetics of Rig-i protein in the indicated
944 Murine bladder cancer cells. The degradation rate of Rig-i protein was quantified by
945 band intensity.

946 **(I)** Western blot revealed the degradation kinetics of RIG-I protein in in the indicated
947 UMUC3 cells. The degradation rate of RIG-I protein was quantified by band intensity.

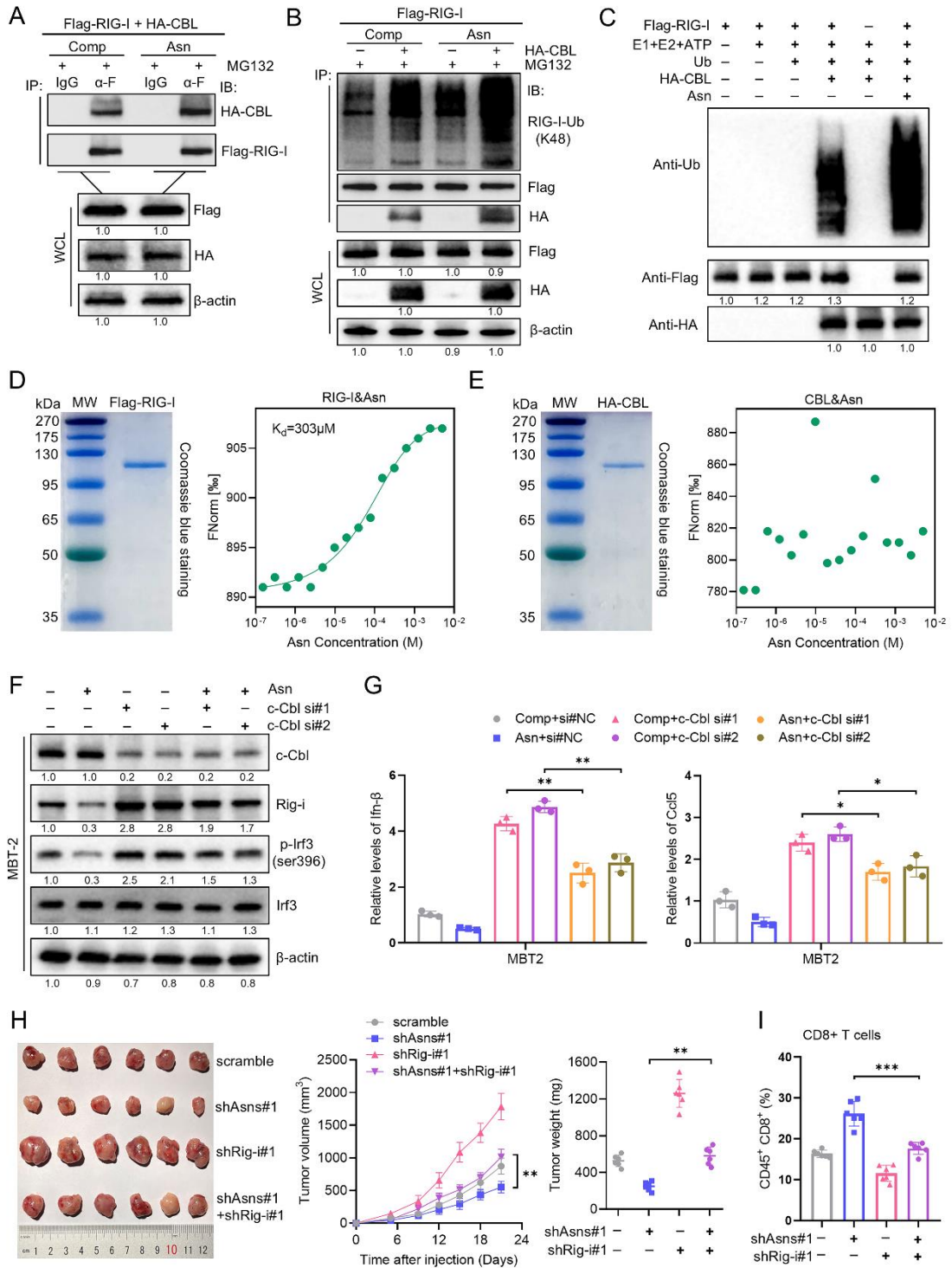
948 **(J)** Western blot analysis showed the Rig-i expression in the indicated MBT2 cells.

949 **(K)** Western blot analysis showed the RIG-I expression in the indicated MB49 or
950 UMUC3 cells.

951 **(L)** HEK293T cells were transfected with Flag-RIG-I and cultured in complete medium
952 (Comp) or medium added Asn (1mM) for 48 h, followed by co-immunoprecipitation
953 and immunoblotting analysis with the indicated antibodies.

954 **(M)** HEK293T cells were transfected with Flag-RIG-I and with scramble or shASNS#1
955 for 48 h, followed by co-immunoprecipitation and immunoblotting analysis with the
956 indicated antibodies.

957 Data were mean \pm SD. Statistical significance was calculated by two tailed unpaired
958 Student's t-tests for A, B, C, D, E, G, H and I. ns, not significant. **p<0.01.



959

960 **Figure 5. Asparagine promotes the CBL-mediated proteasomal degradation of**
 961 **RIG-I.**

962 (A) HEK293T cells were transfected with Flag-RIG-I and HA-CBL and cultured in

963 complete medium (Comp) and medium added Asn (1mM) for 48 h, followed by co-
964 immunoprecipitation and immunoblotting analysis with the indicated antibodies.

965 **(B)** Flag-RIG-I-overexpressed HEK293T cells were cultured in complete medium
966 (Comp) or medium added Asn (1mM), and those co-transfected with a control and HA-
967 CBL overexpression plasmid for 48 h, followed by co-immunoprecipitation and
968 immunoblotting analysis with the indicated antibodies.

969 **(C)** Purified Flag-RIG-I proteins were incubated with the indicated proteins in the
970 presence or absence of 1 mM Asn for 2 h. Mixtures were analyzed by western blot.

971 **(D)** MST measurement of the interaction between Asn and purified RIG-I. Kd value
972 was automatically by the curve fitting.

973 **(E)** MST measurement of the interaction between Asn and purified CBL.

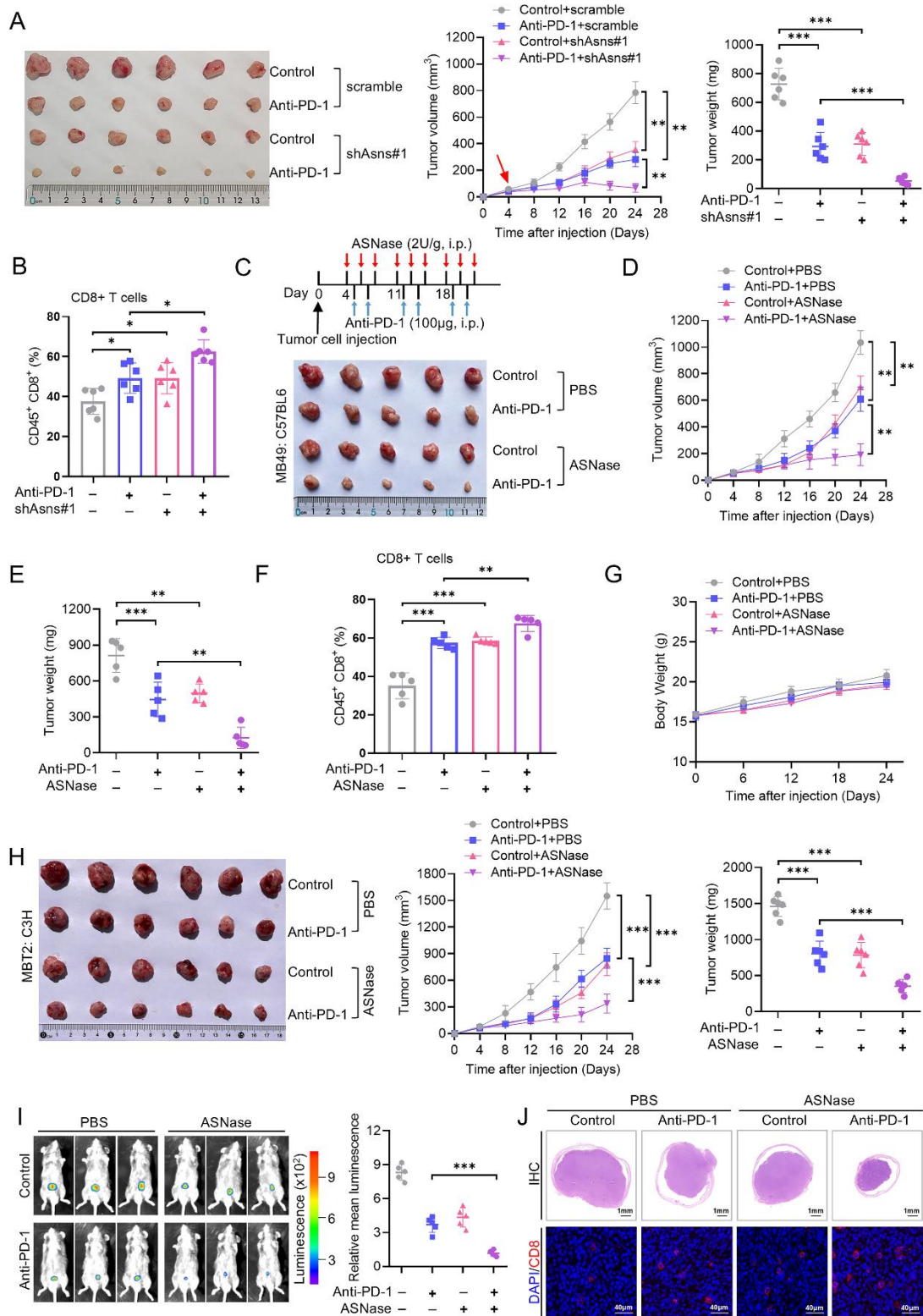
974 **(F)** Western blot of the indicated proteins in MBT2 cells cultured in complete medium
975 (Comp) or medium added Asn (1mM), and those co-transfected with si-NC, si-Cbl#1
976 or si-Cbl#2.

977 **(G)** qRT-PCR revealed the expression levels of Ifn- β and Ccl5 in MBT2 cells cultured
978 in complete medium (Comp) or medium added Asn (1mM), and those co-transfected
979 with si-NC, si-Cbl#1 or si-Cbl#2.

980 **(H)** Tumor growth curves and tumor weight of immunocompetent C3H mice (n = 6)
981 injected subcutaneously with indicated MBT2 cells.

982 **(I)** Tumor infiltrating CD8⁺ T cells from transplanted MBT2 tumors (n = 6) in C3H
983 mice were analyzed by flow cytometry.

984 Data were mean \pm SD. Statistical significance was calculated by two-way ANOVA for
985 G, H and I. *p<0.05, **p<0.01, ***p<0.001.



986

987 **Figure 6. Asparagine restriction overcomes tumor resistance to PD-1 blockade in**
 988 **mouse model.**

989 (A) Tumor growth and tumor weight in immunocompetent C57BL/6 mice injected

990 subcutaneously with MB49 cells stably transfected with scramble and shAsns#1, and
991 treated with anti-PD-1 or isotype control (n = 6).

992 **(B)** Flow cytometry showed the tumor infiltrating CD8⁺ T cells in MB49 tumors of
993 indicated groups.

994 **(C-E)** Schematic of ASNase therapy. Tumor growth and tumor weight in
995 immunocompetent C57BL/6 mice injected subcutaneously with MB49 cells
996 administrated with ASNase, and treated with anti-PD-1 or isotype control (n = 5).

997 **(F)** Tumor infiltrating CD8⁺ T cells in MB49 tumors of indicated groups were analyzed
998 by flow cytometry.

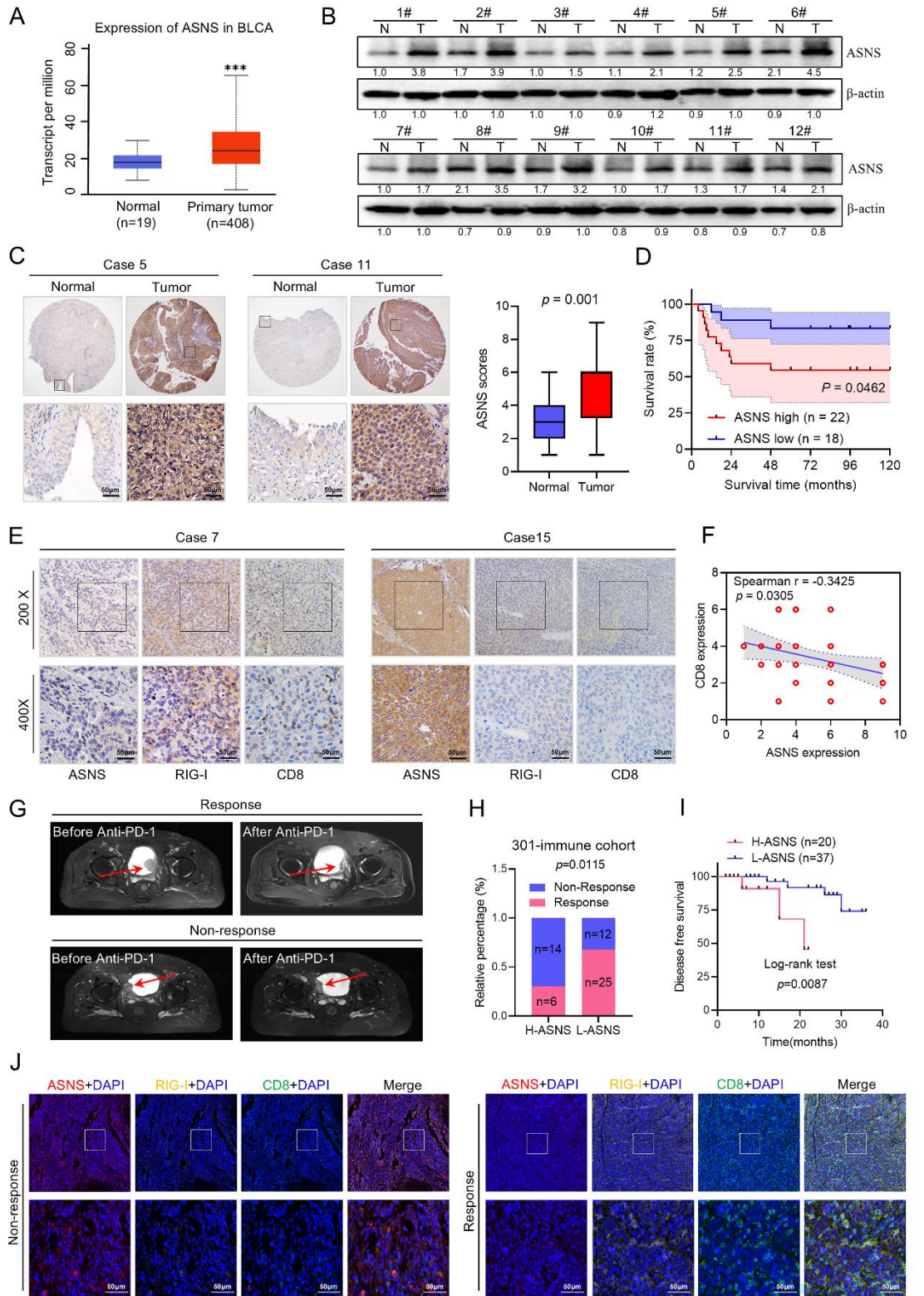
999 **(G)** The body weights among different groups during experimental procedure.

1000 **(H)** Tumor image and tumor weight in immunocompetent C3H mice injected
1001 subcutaneously with MBT2 cells administrated with ASNase, and treated with anti-PD-
1002 1 or isotype control (n = 6).

1003 **(I)** Representative luminescence images and histogram analysis of bioluminescence
1004 intensity in C57BL/6 mice injected orthotopically with luc-labeling MB49 cells with
1005 the treatment of ASNase and anti-PD-1 antibody.

1006 **(J)** Representative hematoxylin and eosin (H&E) staining and immunofluorescence for
1007 CD8 of tumors in the indicated groups. H&E staining, scale bars, 1 mm.
1008 Immunofluorescence staining, scale bars, 40 μ m.

1009 Data were mean \pm SD. Statistical significance was calculated by two-way ANOVA for
1010 A, B, D, E, F, H and I. ns, not significant. *p<0.05, **p<0.01, ***p<0.001.



1011

1012 **Figure 7. Upregulated ASNS leads bladder cancer resistance to ICIs.**

1013 (A) mRNA levels of ASNS in bladder cancer samples from TCGA cohort.

1014 (B) Western blot showed the expression levels of ASNS in our paired samples of

1015 bladder cancer.

1016 **(C)** Representative IHC staining and quantification revealed ASNS expression in paired
1017 samples of bladder cancer from our cohort (n = 40). Scale bar, 50 μ m.

1018 **(D)** Kaplan-Meier analysis of the overall survival of 40 patients with high or low
1019 expression of ASNS.

1020 **(E)** Representative IHC staining of ASNS, RIG-I and CD8 in bladder cancer samples
1021 from our cohort.

1022 **(F)** Correlation analysis of ASNS expression and CD8 expression in bladder cancer
1023 clinical samples (n = 40).

1024 **(G)** Representative MRI image for patient with response and non-response after ICIs
1025 treatment in our hospital (301-immune cohort, n = 57).

1026 **(H)** The relationship between ASNS expression level and immunotherapy efficacy in
1027 301- immune cohort.

1028 **(I)** Disease-free survival of patients with different ASNS IHC scores in our immune
1029 cohort.

1030 **(J)** Representative multi-color IF images for ASNS (red), RIG-I (yellow), CD8 (green)
1031 and DAPI (blue) in response and non-response group patients. Scale bars, 50 μ m.

1032 Data were mean \pm SD. Statistical significance was calculated by two tailed unpaired
1033 Student's t-tests for A. Paired Student's t-tests for C. Chi-square test for H. Survival
1034 analysis of D and I was performed by the log-rank test. ***p<0.001.